IOP Publishing Plasma Phys. Control. Fusion 68 (2026) 015009 https://doi.org/10.1088/1361-6587/ae2b33

Plasma Physics and Controlled Fusion

Check for updates

OPEN ACCESS

RECEIVED
3 September 2025

REVISED
19 November 2025

ACCEPTED FOR PUBLICATION
10 December 2025

PUBLISHED
5 January 2026

PAPER

Evidence of electron microbunching in laser-driven modulated downramp injection and prospects for beam-driven implementation

Chaojie Zhang[1,*], Audrey Farrell[1], Ken A Marsh[1], Qianqian Su[2] and Chan Joshi[1]

[1] Department of Electrical and Computer Engineering, University of California Los Angeles, Los Angeles, CA 90095, United States of America
[2] Department of Physics and Astronomy, University of California Los Angeles, Los Angeles, CA 90095, United States of America
[*] Author to whom any correspondence should be addressed.

E-mail: chaojiez@ucla.edu

Keywords: plasma wakefield acceleration, modulated downramp injection, electron microbunching, free electron laser, particle-in-cell simulation

Abstract

Plasma accelerators can generate high-energy, high-brightness electron beams over centimeter-scale distances, offering novel pathways to compact x-ray free-electron lasers. Generating beams pre-bunched at the desired radiation wavelength would significantly enhance longitudinal coherence and reduce saturation length. Plasma density-modulated downramp injection offers an *in-situ* way to generate such beams with nanometer-scale bunching. Here we report the first experimental evidence of this mechanism in a laser-driven wakefield accelerator, showing that modulated density downramps generate modulated electron energy spectra absent in unmodulated cases. Particle-in-cell simulations reproduce these observations and reveal bunching factors of 0.05 at 0.4 μm, with a compression factor of approximately 7. Building on this demonstration, we propose a beam-driven implementation for FACET-II to generate multi-GeV beams pre-bunched at hundreds of nanometers wavelength, with sub-micrometer emittance, kiloampere peak current, and sub-percent slice energy spread. Two-stage magnetic compression enables tunable bunching from optical to extreme ultraviolet wavelengths while achieving peak currents exceeding 100 kA. Coherent transition radiation calculations confirm diagnostic feasibility. This approach offers a promising path towards compact, high-energy pre-bunched electron sources for advanced photon science applications.

1. Introduction

In a nonlinear plasma accelerator, an intense laser pulse or a high current relativistic charged-particle beam may expel all plasma electrons from its path, leaving a wake that supports accelerating and focusing electric fields exceeding 100 GV m^{-1} [1–3]. This intense wakefield can be used to accelerate self- or externally injected trailing electron bunches to multi-GeV energies over distances of tens of centimeters [4–10], rather than the kilometers required by conventional accelerators [11]. In addition to the large accelerating gradients, plasma accelerators also routinely deliver ultrashort bunches (few to tens of femtoseconds) [12–14] with high-brightness [15] due to the microscopic accelerating structure [16–18] that has favorable longitudinal and transverse electric fields. Such electron bunches are suitable for driving compact free-electron lasers (FELs). Recently, several groups have demonstrated free-electron lasing at optical to EUV wavelengths using electron bunches from plasma accelerators [19–22].

FELs operating in the self-amplified spontaneous emission mode often require long undulators, yet produce radiation with limited temporal coherence [23, 24]. In contrast, pre-bunched electron beams can enable seeded emission growth, thereby reducing the saturation length and improving temporal coherence [25]. External bunching techniques such as high-gain harmonic generation [26, 27] and echo-enabled harmonic generation [28, 29] have been demonstrated in FELs driven by conventional accelerators. However, these techniques add significant complexity and infrastructure requirements, especially when applied to plasma accelerators, as one must carefully match electron bunches between plasma sections and conventional transport beamlines to preserve the small energy spread and high brightness (requiring high peak current and low emittance) that are essential for FELs [30, 31].

An alternative is to directly generate an electron beam that is already bunched in the plasma accelerator and accelerate it to the desired energy. Previous work has demonstrated that microbunching can arise through laser-driven betatron oscillations [32] or phase-dependent ionization injection [33, 34], though these mechanisms produce bunching wavelengths tied to the drive laser parameters with limited independent control. The challenge is how to pre-bunch the electrons on x-ray wavelengths. One promising mechanism is modulated downramp injection, proposed by Xu *et al* [35], which leverages the quasi-linear compressive mapping between spatial modulations in the plasma density downramp and the temporal structure of the injected electron bunch.

In regular downramp injection, as the drive beam traverses the downramp, plasma electrons are continuously injected into the wake as the phase velocity of the trailing edge of the wake drops. Two key effects occur during this injection process: first, a quasi-linear mapping preserves the injection sequence, with electrons injected earlier from upstream positions remaining at the front of the bunch [35]. Second, plasma electrons are compressed during injection since the wake elongation due to plasma density drop is much smaller than the characteristic injection length scale. With a gentle downramp, compression factors- defined as the ratio between the downramp length and the injected bunch length- exceeding 100 can be achieved. When periodic modulations are added to the downramp, the phase velocity of the wake's trailing edge switches between subluminal and superluminal, alternately triggering and ceasing electron injection. This modulated injection, combined with the linear mapping and compression effects, imprints the periodic density modulations onto the current profile of the injected bunch, enabling optical-wavelength plasma modulations to produce x-ray-wavelength electron bunching.

While the physical mechanism of modulated downramp injection has been explored in theory and particle-in-cell simulations, experimental validation has faced challenges across multiple fronts. The first challenge is the generation of reproducible modulated density downramps with precise wavelengths and sufficient modulation magnitude for detectable bunching. The modulation magnitude must be large enough to produce measurable effects yet not so large as to significantly disrupt the wake structure, which would lead to degradation of the emittance of the injected bunch. The modulating wavelengths must be chosen such that injected electrons bunch at wavelengths that can be preserved over the acceleration length despite potential beam quality degradation from betatron motion [36], potential hosing instability [37], and wake evolution [38]. Several methods for creating such periodic plasma structures have been explored, including the use of interfering laser pulses to generate ionization-induced plasma gratings [39, 40], a technique used in this work by superimposing such a grating onto a density downramp to modulate it. Laser-driven implementations face additional constraints: drive laser pulses should be short enough to prevent trailing-edge of the laser pulse to overlap with injected electrons, which may initiate energy exchange between laser fields and injected electrons that degrades bunching quality [41, 42]. For similar reasons, the acceleration length should be optimized so that injected electrons are accelerated to the desired energies while avoiding dephasing effects [43]. Diagnostics pose another significant experimental hurdle. Direct measurement of sub-micrometer electron bunching requires accurate and reliable longitudinal phase space diagnostics with femtosecond or even finer resolution (e.g. transverse deflecting cavities [44]), or coherent radiation measurements that demand precise beam transport and detectors [14]. These challenges explain why, despite promising theoretical predictions, experimental demonstration has remained elusive. Beam-driven plasma wakefield accelerators offer advantages for addressing some of these limitations: they are immune to dephasing and interaction between the injected bunch and the driver, and can provide linear focusing forces ideal for preserving beam quality throughout acceleration if operated in the nonlinear blowout regime [45].

In this paper, we present the first experimental evidence of electron microbunching in laser-driven modulated downramp injection and propose an implementation for beam-driven experiments at FACET-II National User Facility [11]. Section 2 shows evidence of microbunching in laser wakefield acceleration experiments, supported by particle-in-cell simulations. Section 3 presents a beam-driven plasma wakefield design at FACET-II for generating multi-GeV, FEL-quality pre-bunched beams. Section 4 examines post-compression techniques for tuning bunching wavelengths and achieving attosecond bunches with peak currents exceeding 100 kA. Section 5 discusses the feasibility of coherent transition radiation (CTR) as a diagnostic for beam characterization. The final section summarizes findings and implications for future coherent light sources.

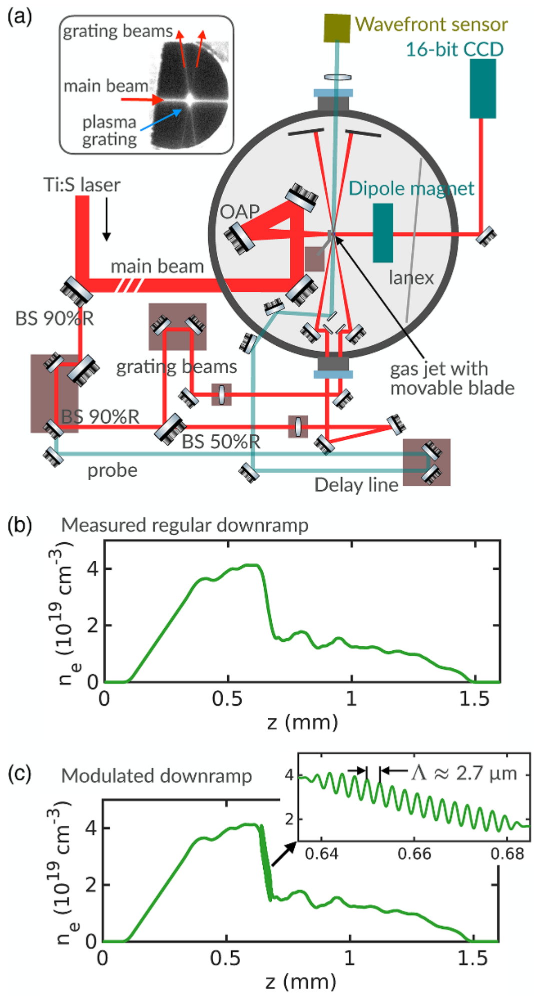

Figure 1. Experimental setup and plasma density profiles. (a) Schematic of the multi-beam laser configuration. A 280 mJ, 35 fs Ti:Sapphire laser pulse is split into a main beam (90%, wake driver), grating beams (9%, plasma grating generation), and probe beam (1%, density diagnostics). The supersonic gas jet is partially blocked by a movable blade to create a density downramp. Electrons are characterized using an energy spectrometer (dipole magnet, Lanex screen, 16-bit camera). The inset shows enhanced plasma scattering indicating grating presence. (b) Representative measured density profile showing a shock-induced downramp from 4×10^{19} to 1.5×10^{19} cm^{-3} over $\sim$40 μm. (c) Modulated downramp created by superimposing the plasma grating, with modulation wavelength $\sim$2.7 μm (schematic illustration; modulation not resolved by wavefront sensor) onto the regular downramp induced by the shock front.

2. Electron microbunching in laser-driven modulated downramp injection

This section presents experimental evidence of microbunching of modulated downramp injected electrons in a laser wakefield accelerator. The experiments were conducted at UCLA using a 10 TW Ti:Sapphire laser system with a multi-beam configuration, where a primary laser pulse drove the plasma wake while two synchronized intersecting beams created a spatially modulated plasma grating through interfering optical field ionization [40]. When this plasma grating was superimposed onto a shock-induced density downramp, we observed distinct periodic modulation in electron energy spectra that was absent without the grating, providing the first experimental evidence of this bunching mechanism.

2.1. Experimental setup

The experimental setup is shown in figure 1(a). A Ti:Sapphire laser system delivers approximately 280 mJ, 35 fs (FWHM) pulses at 800 nm, which are split into multiple beams: 90% of the energy is used as the main beam for driving the wake, while the remaining 10% is further divided into probe diagnostics (1% of total energy) and two identical grating-formation beams (4.5% each, $\sim$12 mJ per beam).

The supersonic helium gas jet, emanating from a 5 mm diameter round nozzle, is partially blocked by a movable blade to create a shock-induced density downramp. The two, equal energy, 800 nm wavelength grating-producing laser beams intersects at $\theta \approx 17°$, creating an interference pattern with wavelength $\Lambda = \frac{\lambda_0}{\left[2\sin\left(\frac{\theta}{2}\right)\right]} \approx 2.7$ μm. The intensity of this interference pattern is just above the ionization threshold of helium atoms and thus helium is singly ionized in regions where the two beams interfere constructively, approximately 20 ps before the arrival of the main beam, to form a plasma grating. During this interval, electrons in the ionized regions begin to move while neutral atoms remain relatively stationary, causing partial diffusion that fills the gaps between ionized regions. When the main beam arrives and fully ionizes the remaining neutral gas, the total density appears modulated due to these earlier plasma grating dynamics [40].

Figure 1(b) shows a representative plasma density profile measured using the probe beam and a wavefront sensor. The density rises nearly linearly to $\sim 4 \times 10^{19}$ cm^{-3}, maintains a $\sim$250 μm plateau, then drops across a $\sim$40 μm downramp to $\sim 1.5 \times 10^{19}$ cm^{-3}. Beyond the shock front, the density continuously decreases to zero over approximately 800 μm. Note that the actual downramp is likely sharper than 40 μm when accounting for shock tilt (i.e. not perfectly vertical), which can broaden the apparent downramp width when retrieving density profiles from the measured probe phase change. Systematic characterization of shock-induced downramps shows that shock widths are typically on the order of 10 c/ω_p, which for this case corresponds to approximately 15 μm [46].

When the grating beams overlap with this downramp region, they create a modulated density structure, schematically illustrated in figure 1(c). The modulation can be eliminated by blocking one or both grating beams. While the wavefront sensor lacks sufficient resolution to directly measure the plasma grating structure, its presence is confirmed by enhanced side-scattering of the grating beams, evident in the plasma light collected by the top-view camera (inset, figure 1(a)).

The main beam is focused by an off-axis parabola to $w_0 \approx 8$ μm (1/e^2 intensity radius), yielding a normalized vector potential $a_0 \approx 1.5$. Particle-in-cell simulations indicate that by the time the main beam reaches the downramp, self-focusing and pulse-compression [47] enable it to drive a nonlinear wake capable of trapping and accelerating plasma electrons. Accelerated electrons are characterized using a non-imaging energy spectrometer consisting of a dipole magnet, Lanex phosphor screen, and 16-bit CCD camera. A thin aluminum foil placed in front of the Lanex screen blocks the residual laser and other scattered light.

2.2. Modulated energy spectra

Direct measurement of electron microbunching typically requires longitudinal phase space diagnostics such as a transverse deflecting cavity that acts as a femtosecond streak camera or analysis of CTR. However, as we already discussed in the introduction section, these approaches present significant technical challenges for plasma accelerators especially if the bunch being characterized is ultrashort and ultrarelativistic.

Given these limitations, we employed analysis of the energy spectrum of the plasma electrons exiting the plasma with and without the micron-period density modulation as an indicator of electron microbunching. This approach leverages the energy chirp typically accumulated by a single electron bunch or multiple longitudinally separated electron bunchlets in laser wakefield accelerators due to non-optimal beam loading, as previously demonstrated by Zhang *et al* [13]. When a beam with a smooth current profile is injected in the case of a regular downramp, the energy spectrum appears as a continuous distribution. Conversely, when temporal bunching occurs during modulated downramp injection, different longitudinal slices experience varying acceleration, mapping the bunched structure onto discrete spectral features. This temporal-to-energy mapping occurs within the plasma during acceleration and is preserved during subsequent vacuum propagation because the electrons are highly relativistic and contain only tens of pC of charge, making spectral analysis a reasonable diagnostic approach.

Figure 2(a) shows electron energy spectra obtained using unmodulated (regular) downramp injection with grating-formation beams blocked. The raw spectra (left panels) exhibit continuous energy distributions, that one would expect from injection in an unmodulated downramp, spanning 15–50 MeV with large energy spread due to energy chirp caused by non-optimal wakefield loading. The linearized spectra (right panels) confirm smooth distributions without distinct peaks. The different spectral shapes are likely due to shot-to-shot variations in beam pointing, energy coupling, and plasma conditions.

Figure 2(b) shows modulated downramp injection effects when grating beams created periodic density variations. Now, the accelerated electron spectra display 2–3 distinct peaks, in contrast to the smooth distributions from regular downramp cases. This energy modulation appears as alternating regions of enhanced and suppressed electron density with peak separated by approximately 5–10 MeV. This periodic energy structure provides experimental evidence of temporal bunching, where the injected electrons have mapped to different phases of the wake that have an increasing accelerating gradient and therefore, they appear at an increasing final energy. As the black dotted line shows in figure 2(b), the charge

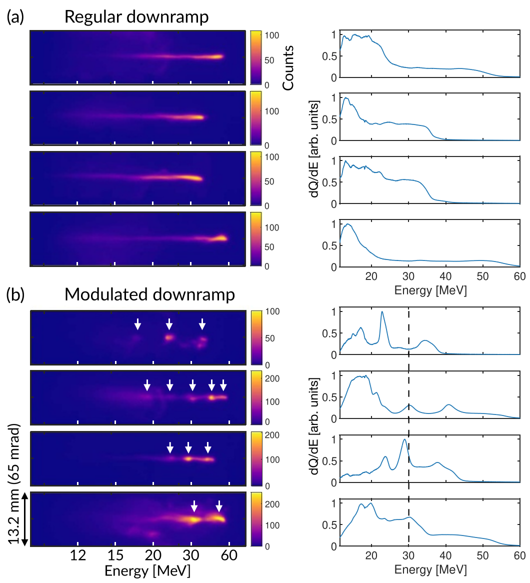

Figure 2. Comparison of energy spectra from density unmodulated (regular) and modulated downramp injection. Each row represents a single-shot measurement, with raw spectrometer images (left) and linearized energy spectra (right). (a) Four representative shots from shock-induced regular downramp injection show characteristic smooth, continuous energy distributions. (b) Four shots obtained when plasma gratings were superimposed on the downramp exhibit clear discrete structure (indicated by white arrows in the raw images) with multiple spectral peaks (e.g. the consistent peak near 30 MeV highlighted by the dashed line), providing experimental evidence consistent with electron microbunching.

bunching at 30 MeV is seen in nearly all the shots, suggesting that the observed structure likely originated from controlled modulated downramp injection rather than random plasma or laser fluctuations.

2.3. Numerical modeling of the experiment

To validate the experimental observations and provide insight into the underlying physics of modulated downramp injection, we have performed particle-in-cell simulations using the OSIRIS [48] code in the quasi-3D configuration. The simulation employed a moving window of $400 \times 160\ c/\omega_0$ in the longitudinal (z) and radial (r) directions, where $2\pi c/\omega_0$ is the laser wavelength, with 8 cylindrical modes in the azimuthal direction. The computational domain was divided into 1600×320 cells with 8 macroparticles per cell.

Two simulations were conducted to compare with the experimental conditions. The first simulation used a regular shock-induced density downramp without modulation (the measured density profile shown in figure 1(b), but with the absolute density reduced by 30% compared to the measured density to better match the experiments), while the second incorporated periodic density modulations with $\delta_n = 0.35 \times 10^{19}\ \mathrm{cm}^{-3}$ amplitude superimposed on the downramp profile (the density profile shown in figure 1(c), also with the peak density reduced by 30%).

Figure 3 presents the simulation results, showing a reasonable agreement with experimental observations. The simulated energy spectrum for the regular downramp case (figure 3(a)) exhibits a continuous distribution, similar to the experimental measurements in figure 2(a). The corresponding longitudinal phase space extracted from the simulation (figure 3(b)) shows a single, continuous electron beam structure with smooth energy-position correlation. The current profile (figure 3(c)) of the injected bunch displays a single peak exceeding 4 kA with a FWHM bunch length of approximately 0.6 μm.

In contrast, the simulation for the modulated downramp injection case (figures 3(d)–(f)) reproduced the key experimental result. The energy spectrum now has multiple distinct peaks, with three clearly visible features indicated by the arrows, similar to the experimental results. More importantly, the longitudinal phase space in figure 3(e) reveals discrete microbunched beamlets separated in the longitudinal direction, with a bunching wavelength of approximately 0.4 μm and clear periodic structure in the current profile (figure 3(f)).

We calculated the bunching factor of the injected beam in both simulation cases. The bunching factor is defined as $b(\lambda) = |\sum_{j=1}^{N} \exp\left(i2\pi z_j/\lambda\right)|/N$, where λ is the bunching wavelength, z_j are electron longitudinal positions, and N is the total number of electrons. For the regular downramp case, the bunching factor at 0.4 μm wavelength was $b(0.4\ \mu\mathrm{m}) \approx 0.02$, primarily attributed to natural variations in the current profile within the short bunch length. For the modulated downramp case, the bunching

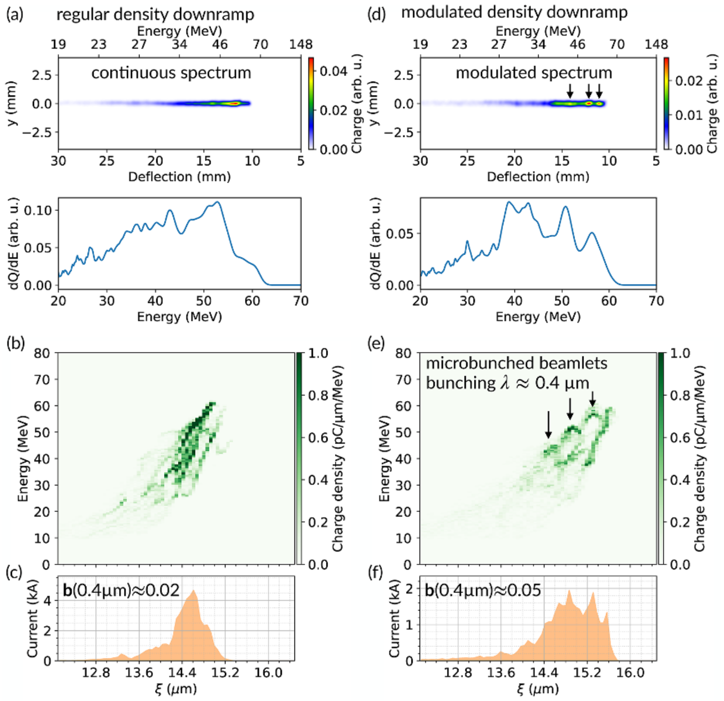

Figure 3. Particle-in-cell simulation validation of modulated downramp injection. (a)–(c) Regular downramp injection showing continuous energy spectrum, smooth longitudinal phase space, and current profile of the bunch. The bunching factor at 0.4 μm $b(0.4\ \mu\text{m}) \approx 0.02$. (d)–(f) Modulated downramp injection with modulation magnitude $\delta_n = 0.35 \times 10^{19}\ \text{cm}^{-3}$ demonstrating spectral modulation and formation of microbunched beamlets with $\sim$0.4 μm separation and enhanced bunching factor $b(0.4\ \mu\text{m}) \approx 0.05$. The microbunching is clearly visible in the longitudinal phase space (e), where the current profile (f) shows multiple distinct peaks with a bunching factor that is approximately 2.5 times larger than the regular downramp case.

factor increased to $b(0.4\ \mu\text{m}) \approx 0.05$, representing a 2.5 times enhancement. The compression factor of approximately 7 was calculated by comparing the 0.4 μm bunching wavelength to the 2.7 μm downramp modulation period. Theoretically, the compression factor is given by $h \approx (r_\text{m} g)^{-1}$, where r_m is the maximum bubble radius, and $g = n_\text{p}^{-1}\left(\text{d}n_\text{p}/\text{d}k_\text{p}z\right)$ is the slope of the downramp [35]. Taking the density profile parameters used in the simulation, we expect a compression factor of 7.4, corresponding to a bunching wavelength of 0.37 μm, which agrees reasonably with the simulated values.

An important limitation of the current experiment was the high plasma density relative to the laser pulse duration. The 35 fs laser pulse, even after self-compression, likely filled the entire wakefield bubble at the lower-shelf density of $\sim 1.5 \times 10^{19}\ \text{cm}^{-3}$, leading to potential interaction between the laser's trailing edge and injected electrons. This interaction may have enabled direct laser acceleration which contributed partially to the observed microbunching, complicating the interpretation of results. However, the systematic differences in longitudinal phase space between simulations with and without downramp modulation—where the presence of the plasma grating was the only variable—suggested that modulated downramp injection was the dominant bunching mechanism. While these results did not provide conclusive proof due to the experimental limitations, both simulations and experiments consistently demonstrated distinct behaviors when the downramp was modulated, providing preliminary evidence of electron microbunching in modulated downramp injection. Further experiments with a shorter laser pulse and/or a lower peak plasma density need to be carried out to conclusively resolve this issue. Another option is to use a highly relativistic electron beam to drive a plasma wakefield accelerator to bypass such complications while accelerating the bunchlets to GeV energies. Such a possibility is considered in the next section.

3. Beam-driven implementation

To overcome the limitations in laser-driven modulated downramp injection described in section 2 and demonstrate modulated downramp injection under more-controlled conditions, we propose a beam-driven plasma wakefield acceleration (PWFA) that we believe is possible at FACET-II. Beam-driven implementations offer several advantages: they are immune to the problematic laser-beam interactions that will adversely affect the beam quality and reduce or destroy the bunching in LWFA with non-optimal length pulses and/or dephasing effects. It is now accepted that high energy electron beam-driven

PWFA can provide linear focusing forces ideal for preserving beam quality if operated in the nonlinear blowout regime, and can also readily achieve higher energies relevant to x-ray FELs. In this section, we present designs supported by PIC simulations to demonstrate that beam-driven modulated downramp injection can generate multi-GeV, high-brightness pre-bunched electron beams with sub-micrometer bunching wavelengths suitable for advanced light source applications.

3.1. Drive beam and plasma source

The FACET-II National User Facility provides electron bunches for beam-driven PWFA studies with energies of 10 GeV in either single- or two-bunch configurations [11]. For the experiment described here, we use the single-bunch configuration of the electron beam. The electron bunch is generated from a photocathode injector, subsequently accelerated through four stages of conventional radio-frequency acceleration sections, and compressed to approximately 20 μm bunch length via three-stage compression using magnetic chicanes. One or more femtosecond current spikes can be created in the bunch through coherent synchrotron radiation with peak currents of up to 100 kA [49]. The bunch can be focused to 15–20 μm spot size using the final focusing system. Previous experiments have confirmed that the intense electric field associated with the focused current spike was sufficient to self-ionize hydrogen/helium gas to form plasma, while the charge contained in the lower-current structure (on the order of 10 kA) of the bunch excited a wake in self-generated meter-scale plasmas [7].

Comprehensive beam diagnostics with sub-percent energy resolution and millimeter-milliradian emittance measurement capabilities have been commissioned [50]. These diagnostics include energy spectrometers covering the 1–30 GeV range, single-shot emittance measurements, and x-ray detectors for betatron dynamics studies. Detailed descriptions of facility capabilities, beam parameters, plasma sources, and diagnostic systems can be found in Storey *et al* [50]. Moreover, a differential pumping system enables gas jet operation in the experimental area without requiring solid windows in the beam path to isolate the gaseous region from the high-vacuum region, which is crucial for preserving the high brightness of both drive and injected electron beams.

We have constructed a 15 cm long, 1 mm wide slit nozzle capable of delivering gas densities around 10^{17} cm^{-3}. An example density profile from fluid simulation is shown in figure 4(a), with the downramp region magnified and depicted in figure 4(b). A density downramp is created by inserting a thin blade into the supersonic gas jet (on the upstream side of the jet with respect to the electron beam). The density drops from 2.2×10^{17} to 1.5×10^{17} cm^{-3} over approximately 300 μm. Following the density downramp, there is a 14-cm uniform region where the gas density remains nearly constant. Beyond the uniform region, there is an exit downramp formed naturally where the density drops to zero over about 1 cm. Similar to the approach described in the previous section, we can modulate the density downramp by superimposing a laser-intensity interference pattern onto the regular density downramp. This will generate a periodic ionization electron grating that evolves into a plasma ion grating as described earlier. The modulation period is chosen to be 8 μm so that the injected electrons bunch at an optical wavelength to facilitate diagnostics. Using a 0.8 μm laser to create such an ionization-induced plasma grating would require an intersecting angle of 0.1 rad between the two grating-producing laser beams. Here we use a small modulation magnitude, but the actual modulation magnitude can be adjusted by tuning the delay between the laser beams and the arrival of the electron drive beam, as shown in [40].

3.2. Simulations of beam-driven modulated downramp injection

We have performed PIC simulations using the density profiles shown in figure 4 with a combination of two codes, OSIRIS [48] and QPAD [51]. The downramp injection process was modeled using OSIRIS in cylindrical coordinates. Subsequently, the 6D phase space of both the drive bunch and the injected bunch was imported into QPAD to continue modeling the remaining acceleration. QPAD uses a quasi-static approximation, allowing us to use a relatively large time step to reduce computational requirements.

In the OSIRIS simulation, we used a moving window with dimensions of $12 \times 6c\omega_p^{-1}$, where c/ω_p^{-1} is the skin depth of plasma at the density of 1.5×10^{17} cm^{-3}. The simulation box was divided into 6912×1152 cells, corresponding to cell sizes of approximately 23.8 and 71.5 nm in the beam propagation and transverse directions, respectively. A time step of 0.000 868 ω_p^{-1} ($\sim$11.9 nm) was used to resolve the injection process. For the drive bunch, 4 particles per cell were initialized, whereas for the pre-ionized plasma electrons, 16 particles per cell were used. The drive bunch had Gaussian distributions in all directions, with $\sigma_z = \sigma_r = 15$ μm and a normalized transverse emittance of 20 μm. The drive bunch contained 1.35 nC of charge and was focused at the edge of the gas jet. The first 1.65 cm of the gas jet (see figure 4(a)) was simulated, which included the sharp injection downramp and approximately 7 mm of acceleration after injection, boosting the injected bunch energy to approximately 350 MeV.

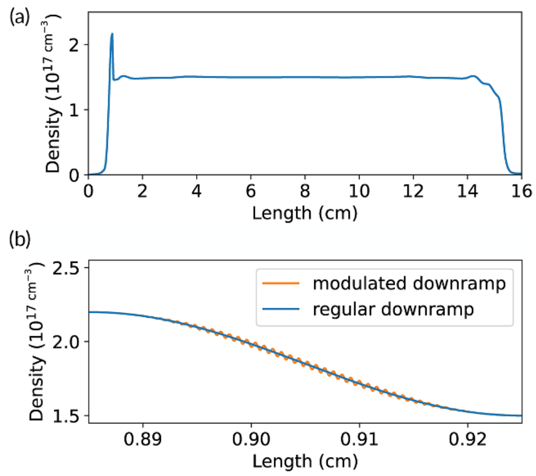

Figure 4. Density profile used in the PIC simulation. (a) Density profile of the 15 cm slit nozzle obtained from fluid simulation. (b) Magnified view of the downramp region. The regular downramp (blue) is created by the shock front, while the modulated downramp (orange) results from superimposing a plasma grating with 8 μm period onto the regular downramp.

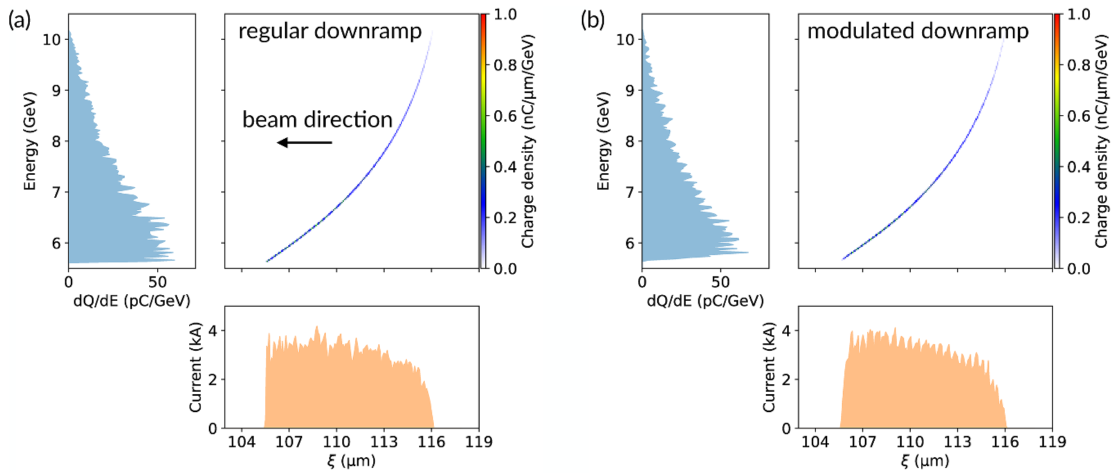

Figure 5. Longitudinal phase space of injected bunches from beam-driven modulated downramp injection. (a) Regular downramp case using the density profile shown in figure 4(b) (blue line). The longitudinal phase space is shown in the top right panel, with the corresponding energy spectrum and current profile depicted in the top left and bottom right panels, respectively. (b) Modulated downramp case using the density profile shown by the orange line in figure 4(b), displaying clear periodic modulation in both the energy spectrum and current profile with ~0.5 μm bunching wavelength.

At the end of the OSIRIS simulation, we extracted the 6D phase space of both the drive and injected bunches and imported them into the QPAD simulation. The QPAD simulation used the same window size and resolution but with a much larger time step (20 ω_p^{-1}), making the simulation ~23 000 times faster than using the OSIRIS code. Yet this time step was sufficiently small to resolve the betatron dynamics of bunches with energies above 100 MeV. The QPAD simulation modeled the acceleration of the downramp-injected electrons until the end of the plasma.

Figure 5 shows the longitudinal phase spaces of the injected bunch, with figure 5(a) depicting the bunch in the regular downramp case (blue line in figures 4(b)) and 5(b) presenting the modulated downramp case (orange line in figure 4(b)). The energy spectrum and current profile of the injected bunch are also displayed alongside the longitudinal phase space.

As shown in figure 5, the overall shape of the longitudinal phase spaces in both cases is extremely similar- the injected bunches have a large energy chirp, covering energies from slightly below 6 GeV to 10 GeV within a FWHM bunch length of approximately 10 μm. The important difference, however, is as expected: in the modulated downramp case, there are regular modulations in the current profile and energy spectrum, compared to the random-peaked structures in the regular downramp case. The

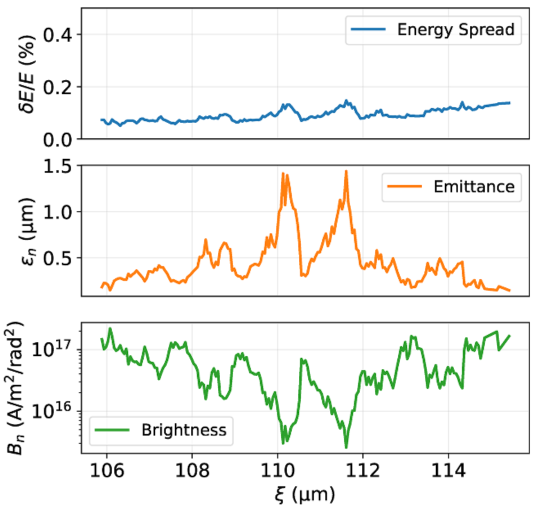

Figure 6. High-quality injected bunch characteristics from modulated downramp injection. (a) Slice energy spread as low as 0.1% across the bunch length. (b) Sub-micrometer slice emittance, with most slices below ∼0.5 μm. (c) Slice brightness approaching 10^{17} A m^{-2} rad^{-2}, superior to state-of-the-art LCLS electron beams.

modulation of the current profile is ∼0.5 μm, corresponding to a compression factor of 16. The bunching factor at this wavelength is approximately 0.02 for the modulated downramp case. The peak current reaches 4 kA and does not vary significantly over the ∼10 μm bunch length.

Figure 6 presents the quality of the injected bunch for the modulated downramp case. Here we show the slice relative energy spread, emittance, and brightness of the bunch. The slice energy spread of the bunch is on the order of 0.1%, corresponding to a spread of only a few MeV within each slice. For most slices, the emittance is below one mm-mrad. Combining the multi-kA peak current and sub-micrometer emittance, the brightness of the injected bunch approaches 10^{17} A m^{-2} rad^{-2}, meaning that the beam is brighter than the state-of-the-art LCLS electron beams. These parameters—including the small slice energy spread, high peak current, and small emittance, together with the 6–10 GeV energy—make the injected bunch suitable for driving x-ray FELs [25].

In the current simulation, the injected electrons bunch at ∼0.5 μm. This choice was made for a practical reason. A bunching wavelength in the optical range is easier to detect. Additionally, the relatively long bunching wavelength makes the energy modulation spacing large enough (∼0.15 GeV) to be readily resolved by electron energy spectrometers, which can serve as the first evidence of microbunching in experiments, similar to the laser-driven experiment described in section 2. Such a large bunching wavelength also eliminates the requirements for resolving x-ray wavelengths and thereby making the simulation computationally manageable. However, previous simulations by Xu *et al* have shown that reducing the modulation period of the downramp to 0.4 μm (by increasing the intersecting angle from 0.1 radian in our case to π radians, namely, using counter-propagating identical laser pulses) can reduce the bunching wavelength of the injected electrons to a few nanometers [35].

4. Two-stage compression to achieve attosecond bunching

It is possible to directly generate electron beams bunched at x-ray wavelengths by using short modulation wavelengths (e.g. 400 nm) on a gentle downramp to achieve very large compression factors [35]. In this section, we show that even starting with a relatively large bunching wavelength, which is more practical for experimental implementation, we can still achieve much shorter bunching wavelengths and larger bunching factors by further compressing the injected beam using a weak magnetic compressor (chicane) that leverages the relatively large energy chirp of the beam [52]. This approach allows us not only to continuously adjust the bunching wavelength, but also to reduce the overall bunch length from tens of femtoseconds to hundreds of attoseconds.

We performed numerical modeling of the compression of the bunch shown in figure 5(b) by calculating the longitudinal phase space of such bunches after traversing a chicane. The final coordinate of a slice in the beam after passing through a chicane is given by $\xi_{\mathrm{f}} = \xi_{\mathrm{i}} + R_{56}\delta - \frac{3}{2}R_{56}\delta^2$, where ξ_{f} and ξ_{i} are the final and initial longitudinal coordinates after and before the chicane, R_{56} is the longitudinal dispersion of the chicane, and $\delta = (E - E_0)/E_0$ is the relative energy deviation with E_0 as the reference energy. Here we use $E_0 = 7$ GeV.

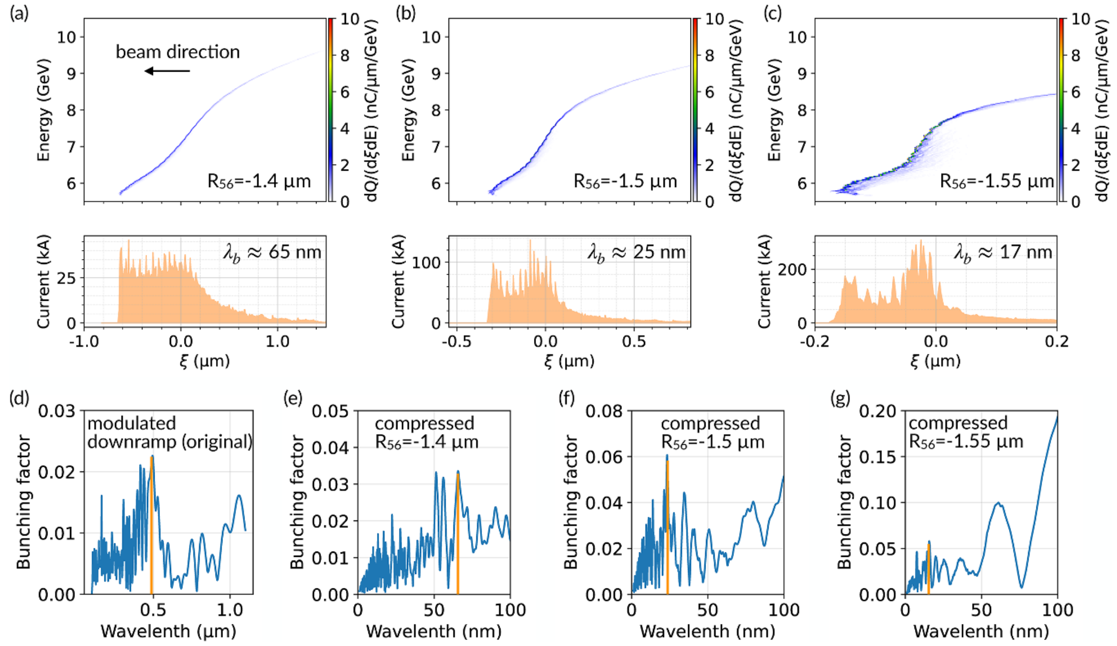

Figure 7. Continuous tuning of bunching wavelength by compressing the pre-bunched beam. (a)–(c) Longitudinal phase spaces calculated by compressing the beam shown in figure 5(b) using a chicane with different longitudinal dispersions R_{56}. The bunching wavelength is reduced from $\sim$0.5 μm to 65, 25, and 17 nm in these cases, respectively, while peak currents increase from 4 kA to 40, 100, and >200 kA. (d) Bunching factor of the injected beam before compression. (e)–(g) Bunching factors of the compressed beam with different compression strengths. The orange lines mark peaks corresponding to the bunching wavelengths visible in the current profiles.

The results are shown in figure 7. The longitudinal phase space of the injected bunch after compression is presented in figures 7(a)–(c), each corresponding to a different compression strength (longitudinal dispersion) of the chicane. After compression, the bunching wavelength is reduced from $\sim$0.5 μm to 65 nm in figure 7(a), and down to 17 nm in figure 7(c). Due to compression, the peak current also increases from 4 kA to 40 kA in figure 7(a) and eventually exceeds 200 kA in the extreme compression case shown in figure 7(c). The FWHM bunch length is reduced from $\sim$10 μm to 0.2 μm. The modulation magnitude is also enhanced, as clearly shown in figure 7(b) where the modulation magnitude (peak to valley) in the current profile approaches the average peak current.

We then calculated the bunching factor as a function of wavelength for these different cases, with results shown in figures 7(d)–(g). Before compression, the injected electrons bunch at $\sim$0.5 μm with a bunching factor of $\sim$0.02, as depicted in figure 7(d). After compression, the bunching wavelength is reduced and the bunching factor increases to 0.03 in (e) and $\sim$0.06 in (f) and (g). In the extreme compression case shown in (g), there is another peak at $\sim$60 nm with a bunching factor reaching 0.1, which results from nonlinearities in both the original longitudinal phase space (nonlinear energy chirp) and the chicane compression that lead to the emergence of a different bunching wavelength. The even larger bunching factor at longer wavelengths is due to the fact that the entire bunch is compressed to hundreds of attoseconds, causing nearly all electrons to radiate coherently at long wavelengths.

The continuous variation of bunching wavelength and magnitude using a small chicane shown in figure 7 provides a practical approach to manipulate the beam. It also demonstrates that because of the large energy chirp, it is possible to compress the bunch to attosecond scales, thereby significantly increasing the peak current and peak power of the bunch to create extreme beams.

5. Diagnostics

In this section, we briefly discuss the feasibility of diagnosing the micro- to nano-scale bunching of modulated downramp injected electrons. As already shown in figures 2(b) and 5(b), the energy spectrum of the injected bunch contains regularly spaced peaks due to the modulation of the current profile and the large energy chirp. This can potentially serve as the first experimental observable of discretized injection in the wake. We note that there may be potential overlap between the energy spectrum of the drive bunch that has lost energy and the injected bunch that has gained several GeV energies, which could complicate the isolation of the injected bunch signal. This can be overcome by keeping the

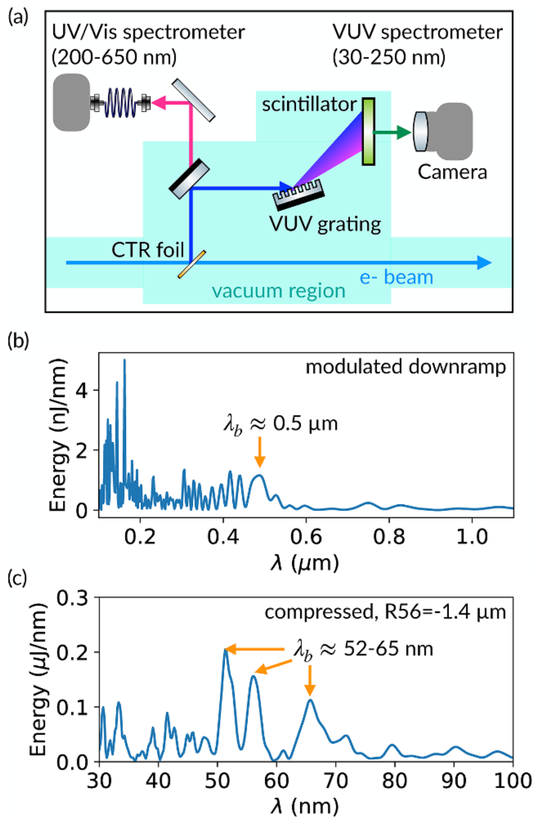

Figure 8. Spectral diagnostics for modulated downramp injected electrons. (a) Schematic of the Vis-VUV spectrometer setup at FACET-II. (b) Calculated coherent transition radiation spectrum using electrons from PIC simulations (figure 5(b)), showing a clear peak at 0.5 μm corresponding to the bunching wavelength. (c) CTR spectrum of the compressed bunch with $R_{56} = -1.4$ μm (figures 7(a) and (e)). The bunching wavelength has been reduced to ∼65 nm, and the spectrum shows three prominent peaks spanning 52–65 nm, corresponding to the peaks visible in the bunching factor plot. Each peak contains several microjoules of energy.

plasma length short enough that the decelerating drive beam electrons do not overlap with the accelerating electrons.

A more decisive diagnostic for measuring the bunched electrons is to measure the coherent radiation generated by them when they traverse metallic foil and emit transition radiation [14, 53]. As shown in figure 7, the injected electrons are bunched at approximately 0.5 μm, and the bunching wavelength can be further reduced to tens of nanometers by sending the bunch through a small chicane. Such bunched electrons emit CTR which scales as square of the number of particles contained within a wavelength of a particular wavelength radiation and not as the number of electrons as normal transition radiation. To diagnose the CTR generated by such bunches, a spectrometer covering VUV to visible wavelengths has been installed and commissioned at FACET-II.

The schematic of the spectrometer setup is shown in figure 8(a). Both the drive and injected electrons are refocused by quadrupoles onto a CTR foil (e.g. a polished thin metallic foil). Note that when the drive electron energies do not overlap with the injected electrons, focusing the injected electrons will cause the drive electrons to be out of focus, corresponding to a larger spot size that avoids damaging the foil and suppresses their potential contribution to the radiation. The radiation primarily generated by the injected electrons is directed to either a UV/Vis spectrometer covering the 200–650 nm wavelength range or an in-vacuum, grating-based VUV spectrometer covering the 30–250 nm wavelength range.

We have performed CTR calculations using the bunch from PIC simulations, and the results are shown in figures 8(b) and (c). In this calculation, the 6D phase space of the injected electrons was used. The radiation at a virtual detector placed 20 cm away from the radiation source (an ideal metal CTR foil) was calculated by coherently summing (taking account of electric field phase and amplitude) the radiation generated by each particle as it traverses the radiator to obtain the overall field. Once the overall field at the virtual detector was obtained, a Fourier transform provided its spectrum. The calculated spectrum for the injected electron bunch from the modulated downramp shown in figure 5(b) is depicted in figure 8(b). A clear peak appears at 0.5 μm, as expected from the 0.5 μm bunching wavelength (see the peak in the bunching factor plot in figure 7(d)). There are noisy peaks at shorter wavelengths, which result from shot noise due to the limited number (∼half million) of macroparticles and should be largely suppressed in actual measurements. For comparison, we show in figure 8(c) the CTR spectrum of a compressed bunch—specifically, the downramp injected electrons after passing through a small chicane with R_{56} of -1.4 μm (see figure 7(e)). In this case, the bunch was compressed and the bunching wavelength was reduced from 0.5 μm to ∼65 nm. There are three prominent peaks in the bunching factor plot shown in figure 7(e). Similarly, the calculated CTR spectrum also show three large peaks spanning 52–65 nm. Each peak contains a few microjoules of energy, corresponding to a sufficient number of photons for detection.

6. Summary

We have presented the first experimental evidence of electron microbunching through modulated downramp injection in laser wakefield acceleration. By modulating the shock-induced density downramp with an ionization induced plasma grating, we observed distinct modulation in electron energy spectra that was absent in regular downramp cases. Particle-in-cell simulations reproduced these experimental observations and revealed bunching factors of 0.05 at 0.4 μm wavelengths with compression factors of approximately 7 for the laser-driven case.

Building on these proof-of-concept results, we have developed a beam-driven implementation design for FACET-II that addresses the limitations of laser-driven approaches while scaling to multi-GeV energies. PIC simulations demonstrate that this approach can generate high-brightness pre-bunched electron beams with sub-micrometer emittance, kiloampere peak current, and sub-percent slice energy spread suitable for seeded x-ray FELs and CTR. The addition of magnetic compressor enables continuous tuning of bunching wavelength from optical to extreme ultraviolet regimes while achieving peak currents exceeding 200 kA and bunching factors of 0.1. CTR calculations confirm the feasibility of definitive bunching characterization using existing FACET-II diagnostics. This work provides a promising path toward compact, high-energy pre-bunched electron sources that could significantly enhance the performance of plasma-accelerator-driven coherent light sources, by enabling seeded operation with improved temporal coherence and reduced saturation lengths.

Data availability statement

The data cannot be made publicly available upon publication because they are not available in a format that is sufficiently accessible or reusable by other researchers. The data that support the findings of this study are available upon reasonable request from the authors.

Acknowledgment

This work was supported by the U.S. Department of Energy Grant DE-SC0010064, and funding from UCLA. The simulations were performed on the Energy Research Scientific Computing Centre (NERSC) Perlmutter cluster operated under Contract No. DE-AC02-5CH11231 at Lawrence Berkeley National Laboratory (LBNL).

ORCID iDs

Chaojie Zhang 0000-0001-8035-3014
Audrey Farrell 0000-0003-1328-3145
Ken A Marsh 0000-0002-2929-3682
Qianqian Su 0000-0003-1377-8914
Chan Joshi 0000-0002-1696-9751

References

[1] Tajima T and Dawson J M 1979 Laser electron accelerator *Phys. Rev. Lett.* **43** 267
[2] Chen P, Dawson J M, Huff R W and Katsouleas T 1985 Acceleration of electrons by the interaction of a bunched electron beam with a plasma *Phys. Rev. Lett.* **54** 693
[3] Joshi C 2006 Plasma accelerators *Sci. Am.* **294** 40
[4] Faure J, Glinec Y, Pukhov A, Kiselev S, Gordienko S, Lefebvre E, Rousseau J-P, Burgy F and Malka V 2004 A laser–plasma accelerator producing monoenergetic electron beams *Nature* **431** 541
[5] Geddes C G R, Toth C, van Tilborg J, Esarey E, Schroeder C B, Bruhwiler D, Nieter C, Cary J and Leemans W P 2004 High-quality electron beams from a laser wakefield accelerator using plasma-channel guiding *Nature* **431** 538
[6] Mangles S P D *et al* 2004 Monoenergetic beams of relativistic electrons from intense laser–plasma interactions *Nature* **431** 535
[7] Zhang C *et al* 2024 Generation of meter-scale hydrogen plasmas and efficient, pump-depletion-limited wakefield excitation using 10 GeV electron bunches *Plasma Phys. Control. Fusion* **66** 025013

[8] Picksley A *et al* 2024 Matched guiding and controlled injection in dark-current-free, 10-GeV-Class, channel-guided laser-plasma accelerators *Phys. Rev. Lett.* **133** 255001
[9] Blumenfeld I *et al* 2007 Energy doubling of 42 GeV electrons in a metre-scale plasma wakefield accelerator *Nature* **445** 741
[10] Litos M *et al* 2014 High-efficiency acceleration of an electron beam in a plasma wakefield accelerator *Nature* **515** 7525
[11] Yakimenko V *et al* 2019 FACET-II facility for advanced accelerator experimental tests *Phys. Rev. Accel. Beams* **22** 101301
[12] Lundh O *et al* 2011 Few femtosecond, few kiloampere electron bunch produced by a laser–plasma accelerator *Nat. Phys.* **7** 219
[13] Zhang C J *et al* 2016 Temporal characterization of ultrashort linearly chirped electron bunches generated from a laser wakefield accelerator *Phys. Rev. Accel. Beams* **19** 062802
[14] LaBerge M *et al* 2024 Revealing the three-dimensional structure of microbunched plasma-wakefield-accelerated electron beams *Nat. Photon.* **18** 952
[15] Wang W T *et al* 2016 High-brightness high-energy electron beams from a laser wakefield accelerator via energy chirp control *Phys. Rev. Lett.* **117** 124801
[16] Matlis N H *et al* 2006 Snapshots of laser wakefields *Nat. Phys.* **2** 749
[17] Sävert A *et al* 2015 Direct observation of the injection dynamics of a laser wakefield accelerator using few-femtosecond shadowgraphy *Phys. Rev. Lett.* **115** 055002
[18] Zhang C J *et al* 2017 Femtosecond probing of plasma wakefields and observation of the plasma wake reversal using a relativistic electron bunch *Phys. Rev. Lett.* **119** 064801
[19] Wang W *et al* 2021 Free-electron lasing at 27 nanometres based on a laser wakefield accelerator *Nature* **595** 516
[20] Pompili R *et al* 2022 Free-electron lasing with compact beam-driven plasma wakefield accelerator *Nature* **605** 659
[21] Labat M *et al* 2022 Seeded free-electron laser driven by a compact laser plasma accelerator *Nat. Photon.* **17** 150–6
[22] Barber S K *et al* 2025 Greater than 1000-fold gain in a free-electron laser driven by a laser-plasma accelerator with high reliability *Phys. Rev. Lett.* **135** 055001
[23] Emma P *et al* 2010 First lasing and operation of an ångstrom-wavelength free-electron laser *Nat. Photon.* **4** 641–7
[24] Bostedt C, Boutet S, Fritz D M, Huang Z, Lee H J, Lemke H T, Robert A, Schlotter W F, Turner J J and Williams G J 2016 Linac coherent light source: the first five years *Rev. Mod. Phys.* **88** 015007
[25] Pellegrini C, Marinelli A and Reiche S 2016 The physics of x-ray free-electron lasers *Rev. Mod. Phys.* **88** 015006
[26] Yu L H 1991 Generation of intense uv radiation by subharmonically seeded single-pass free-electron lasers *Phys. Rev. A* **44** 5178
[27] Huang Z and Kim K-J 2007 Review of x-ray free-electron laser theory *Phys. Rev. Accel. Beams* **10** 034801
[28] Xiang D and Stupakov G 2009 Echo-enabled harmonic generation free electron laser *Phys. Rev. Accel. Beams* **12** 030702
[29] Zhao Z T *et al* 2012 First lasing of an echo-enabled harmonic generation free-electron laser *Nat. Photon.* **6** 360
[30] Xu X L *et al* 2016 Physics of phase space matching for staging plasma and traditional accelerator components using longitudinally tailored plasma profiles *Phys. Rev. Lett.* **116** 124801
[31] Lindstrøm C A *et al* 2024 Emittance preservation in a plasma-wakefield accelerator *Nat. Commun.* **15** 6097
[32] Németh K, Shen B, Li Y, Shang H, Crowell R, Harkay K C and Cary J R 2008 Laser-driven coherent betatron oscillation in a laser-wakefield cavity *Phys. Rev. Lett.* **100** 095002
[33] Xu X L *et al* 2016 Nanoscale electron bunching in laser-triggered ionization injection in plasma accelerators *Phys. Rev. Lett.* **117** 034801
[34] Deng A, Li X, Luo Z, Li Y and Zeng J 2023 Generation of attosecond micro bunched beam using ionization injection in laser wakefield acceleration *Opt. Express* **31** 19958
[35] Xu X, Li F, Tsung F S, Miller K, Yakimenko V, Hogan M J, Joshi C and Mori W B 2022 Generation of ultrahigh-brightness prebunched beams from a plasma cathode for x-ray free-electron lasers *Nat. Commun.* **13** 3364
[36] San Miguel Claveria P *et al* 2019 Betatron radiation and emittance growth in plasma wakefield accelerators *Phil. Trans. R. Soc. A* **377** 20180173
[37] Huang C *et al* 2007 Hosing instability in the blow-out regime for plasma-wakefield acceleration *Phys. Rev. Lett.* **99** 255001
[38] Guillaume E *et al* 2015 Electron rephasing in a laser-wakefield accelerator *Phys. Rev. Lett.* **115** 155002
[39] Yu L-L, Sheng Z-M and Zhang J 2009 Plasma Bragg density gratings produced by optical-field ionization *J. Opt. Soc. Am. B* **26** 2095
[40] Zhang C, Nie Z, Wu Y, Sinclair M, Huang C-K, Marsh K A and Joshi C 2021 Ionization induced plasma grating and its applications in strong-field ionization measurements *Plasma Phys. Control. Fusion* **63** 095011
[41] Cipiccia S *et al* 2011 Gamma-rays from harmonically resonant betatron oscillations in a plasma wake *Nat. Phys.* **7** 867
[42] Shaw J L, Lemos N, Amorim L D, Vafaei-Najafabadi N, Marsh K A, Tsung F S, Mori W B and Joshi C 2017 Role of direct laser acceleration of electrons in a laser wakefield accelerator with ionization injection *Phys. Rev. Lett.* **118** 064801
[43] Debus A, Pausch R, Huebl A, Steiniger K, Widera R, Cowan T E, Schramm U and Bussmann M 2019 Circumventing the dephasing and depletion limits of laser-wakefield acceleration *Phys. Rev. X* **9** 031044
[44] Behrens C *et al* 2014 Few-femtosecond time-resolved measurements of x-ray free-electron lasers *Nat. Commun.* **5** 3762
[45] Clayton C E *et al* 2016 Self-mapping the longitudinal field structure of a nonlinear plasma accelerator cavity *Nat. Commun.* **7** 12483
[46] Zhang C, Huang C-K, Marsh K A, Xu X L, Li F, Hogan M, Yakimenko V, Corde S, Mori W B and Joshi C 2019 Effect of fluctuations in the down ramp plasma source profile on the emittance and current profile of the self-injected beam in a plasma wakefield accelerator *Phys. Rev. Accel. Beams* **22** 111301
[47] Esarey E, Schroeder C B and Leemans W P 2009 Physics of laser-driven plasma-based electron accelerators *Rev. Mod. Phys.* **81** 1229
[48] Fonseca R A 2002 OSIRIS: a three-dimensional, fully relativistic particle in cell code for modeling plasma based accelerators *Computational Science—ICCS 2002* vol 2331, ed P M A Sloot *et al* (Springer) pp 342–51
[49] Emma C *et al* 2025 Experimental generation of extreme electron beams for advanced accelerator applications *Phys. Rev. Lett.* **134** 085001
[50] Storey D *et al* 2024 Wakefield generation in hydrogen and lithium plasmas at FACET-II: diagnostics and first beam-plasma interaction results *Phys. Rev. Accel. Beams* **27** 051302
[51] Li F, An W, Decyk V K, Xu X, Hogan M J and Mori W B 2021 A quasi-static particle-in-cell algorithm based on an azimuthal Fourier decomposition for highly efficient simulations of plasma-based acceleration: QPAD *Comput. Phys. Commun.* **261** 107784
[52] Emma C, Xu X, Fisher A, Robles R, MacArthur J P, Cryan J, Hogan M J, Musumeci P, White G and Marinelli A 2021 Terawatt attosecond x-ray source driven by a plasma accelerator *APL Photonics* **6** 076107
[53] Lumpkin A H *et al* 2020 Coherent optical signatures of electron microbunching in laser-driven plasma accelerators *Phys. Rev. Lett.* **125** 014801